# Tunable topological phase transition from nodal-line semimetal to Weyl semimetal by breaking symmetry

Jing Li, Hailong Wang,* and Hui Pan†
*Department of Physics, Beihang University, Beijing 100191, China*

(Received 26 October 2021; accepted 3 December 2021; published 20 December 2021)

In this paper, we theoretically study the topological phase transition from nodal-line semimetal to Weyl semimetal. The nodal-line structure is protected by mirror symmetry and located on the $k_x$-$k_y$ mirror reflection plane, and the Hamiltonian of nodal-line semimetal has an emergent chiral symmetry on this plane. When the mirror symmetry is broken, the topological nodal line opens the gap and the nodal-line semimetal transition to Weyl semimetal with Weyl points on the $k_x$ axis or the $k_y$ axis. In addition, we break the chiral symmetry and realize the Weyl semimetal with the Weyl points on the $k_z$ axis. Destruction of the chiral symmetry leads to the gradual bending of the energy bands. With the evolution of the energy bands, the type-II nodal-line semimetal, the type-II Weyl semimetal and the type-I Weyl semimetal are successively realized. Furthermore, we also study the surface states of the nodal-line semimetal and the corresponding Weyl semimetals after the phase transition. Our work provides more ways to study the phase transition between nodal-line semimetal and Weyl semimetal and helps realize possible applications in topological electronic devices in the future.

DOI: 10.1103/PhysRevB.104.235136

## I. INTRODUCTION

Topological semimetals have attracted profound research due to their nontrivial topological quantum states and transport properties [1–12]. According to the crossing of conduction and valence bands, topological semimetals could be classified into Dirac semimetals (DSMs) [13–16], Weyl semimetals (WSMs) [17–19], nodal-line semimetals (NLSMs) [20–24], and nodal-surface semimetals (NSSMs) [25–29]. Compared with DSMs and WSMs that have discrete points at the intersection of conduction and valence bands in momentum space, the NLSMs are characterized by forming the protected one-dimensional nodal line or closed loop at the intersection of energy bands [30–32]. In NSSMs, the conduction and valence bands touch each other on two-dimensional nodal surface in the Brillouin zone [27,28]. In recent years, NLSMs have been theoretically predicted in many materials [21,22,33–40], some of which have been experimentally confirmed by angle-resolved photoelectron spectroscopy (ARPES) in ZrSiS [41,42], $Cu_2Si$ [43], CuSe [44], and $GdAg_2$ [45].

The nontrivial topological structure of the energy band intersection points of the DSMs and WSMs in the momentum space result in the surface Fermi arc state, which connects two Weyl points with opposite chirality on the projection plane [46]. In NLSMs, these surface states appear in the form of a drum-head-like flat, which is bounded by the nodal lines of the projection surface [35]. DSMs can be obtained in system with time-reversal and inversion symmetry. Breaking the symmetry of time-reversal or inversion reversal can realize the topological phase transition from DSMs to WSMs [47]. Unlike DSMs and WSMs, the topological stability of NLSMs requires more symmetries. According to symmetry protection, NLSMs can usually be divided into two types. One type is protected by both time-reversal and inversion symmetry, and the other is protected by mirror symmetry with the nodal ring located on the mirror reflection plane [47,48]. With some symmetry breaking, NLSMs will be transformed into other exotic topological phases, such as topological insulators and nodal-point semimetals (DSMs and WSMs). The spin-orbit coupling (SOC) can destroy the symmetries of NLSM. When SOC is present, the nodal line in CaAgAs disappears and a band gap is induced [49], the nodal ring in HfC turns into Weyl points [24] and the nodal ring in CaTe evolve into Dirac points [50]. In the present work we focus on the NLSM with mirror symmetry [51]. The nodal line is located on the mirror reflection plane, and in this mirror plane the Hamiltonian has an emergent chiral symmetry. Recently, it is theoretically predicted that nodal line can be realized in some magnetic oxides [52], $MnF_3$ [53], magnetic GdSbTe [54], $\beta - Fe_2PO_5$ [55], and $LiTi_2O_4$ [56].

In this work we study the topological phase transition from NLSM to WSM based on band structure calculations and symmetry analysis. We employ an effective model [51], which is formed by introducing magnetic extension on the basis of Dirac equation model [57]. This theoretical model can be adapted to different ferromagnetic materials by adjusting parameters, such as $HgCr_2Se_4$ [58], $Co_2TiX$ ($X$ = Si, Ge, or Sn) [59], and Heusler compounds $Fe_2MnX$ ($X$ = P, As, Sb) [60]. First, we introduce two perturbations that can break the mirror symmetry, leading to the destruction of the nodal ring in $k_x$-$k_y$ plane, producing WSMs with Weyl points along the $k_x$ axis and with Weyl points along the $k_y$ axis, respectively. Second, we break the chiral symmetry and realize the WSM with two

*hlwang@buaa.edu.cn
†hpan@buaa.edu.cn

 

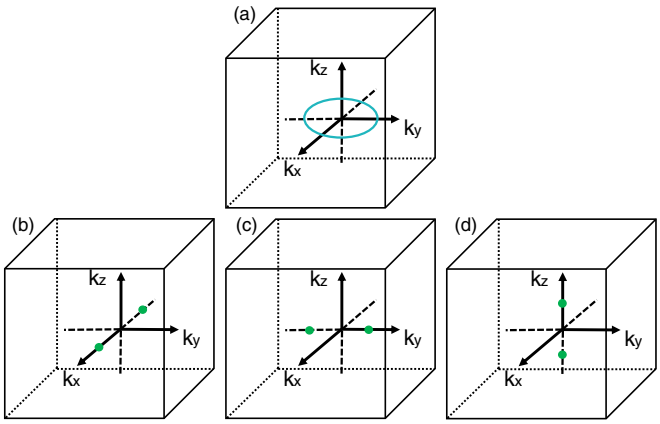


FIG. 1. (a) The location of the nodal line in the $k_x$-$k_y$ plane without the perturbation term in the Brillouin zone. (b), (c) The locations of the Weyl points along the $k_x$ axis and along the $k_y$ axis with the perturbation terms that break the mirror symmetry. (d) The locations of the Weyl points along the $k_z$ axis with the perturbation term that breaks the chiral symmetry.

Weyl points along the $k_z$ axis. In particular, we realize a series of topologically nontrivial phases in the process of adjusting the perturbation term that destroys the chiral symmetry. The perturbation term causes the band to bend and the nodal ring gradually becomes smaller and forms the type-II nodal-line semimetal, which then shrinks to a nodal point. As the perturbation continues to increase, two Weyl points are split in the $k_z$ direction, realizing the topological phase transition to the type-II Weyl semimetal, and eventually forming the type-I Weyl semimetal. Figure 1(a) shows the position of nodal ring in the $k_x$-$k_y$ plane in the Brillouin zone before phase transition. The perturbation terms are introduced to realize the topological phase transformation to three different WSMs, and the Weyl points positions are shown in Figs. 1(b), 1(c), and 1(d), respectively.

Our paper is organized as follows. In Sec. II, we introduce the low-energy effective model of the NLSM [51] and the symmetries. In Sec. III, we introduce two perturbation terms to break the mirror symmetry, and realize the topological phase transition from NLSM to WSM. In Sec. IV, we consider introducing a perturbation term that destroys the chiral symmetry and realizes the topological phase transition to the WSM. We also study the surface states of the nodal-line semimetal and the corresponding Weyl semimetals after the phase transition. Finally, we give our conclusion in Sec. V.

## II. MODEL HAMILTONIAN

We introduce a simple four-band model to describe the NLSM on a cubic lattice, which is expressed as the following Hamiltonian [51]:

$$\mathcal{H}(\mathbf{k}) = (mc^2 - M\mathbf{k}^2)\tau_z \otimes \sigma_0 + ck_x\tau_x \otimes \sigma_x + ck_y\tau_x \otimes \sigma_y + ck_z\tau_x \otimes \sigma_z + B\tau_z \otimes \sigma_z. \quad (1)$$

Here, $\mathbf{k} = (k_x, k_y, k_z)$ is the momentum vector ($\mathbf{k}^2 = k_x^2 + k_y^2 + k_z^2$), and the Pauli matrices $\tau_i$ and $\sigma_i$ $(i = x, y, z)$ are acting on the spin and the orbital degree of freedom, respectively. $\tau_0$ and $\sigma_0$ are the identity matrices. $m$, $M$, and $c$ are the model parameters. $B$ is an exchange field, and this term breaks the time-reversal symmetry $\mathcal{T}$ and leads to the phase transition from topological insulator to NLSM [51]. The time-reversal symmetry is implemented by $\mathcal{T} = i\tau_0 \otimes \sigma_y\mathcal{K}$, where $\mathcal{K}$ is the complex conjugation. The inversion symmetry is $\mathcal{P} = \tau_z \otimes \sigma_0$. The diagonalization of the Hamiltonian in Eq. (1) produces four-band dispersion

$$E_{s,r}(\mathbf{k}) = s\Big[B^2 + (mc^2 - M\mathbf{k}^2)^2 + c^2\mathbf{k}^2 + 2rB\sqrt{(mc^2 - M\mathbf{k}^2)^2 + c^2\left(k_x^2 + k_y^2\right)}\Big]^{\frac{1}{2}}, \quad (2)$$

where $s = \pm$, $r = \pm$. The bands touching can be achieved by solving $E_{s,r}(\mathbf{k}) = 0$. We can get that the nodal line of the band touch is located in the $k_z = 0$ plane, which is determined by the formula $M^2(k_x^2 + k_y^2)^2 + (2mc^2M - c^2)(k_x^2 + k_y^2) - B^2 + m^2c^4 = 0$. The nodal line is protected by the mirror symmetry $\mathcal{M}_z$ in the $k_z = 0$ plane, where $\mathcal{M}_z = i\tau_z \otimes \sigma_z$. In the mirror plane, the Hamiltonian in Eq. (1) has an emergent chiral symmetry $\mathcal{C}$, $\{\mathcal{H}(\mathbf{k}), \mathcal{C}\} = 0$, where $\mathcal{C} = i\tau_x \otimes \sigma_z$. The chiral symmetry is a combination of time-reversal symmetry and particle-hole symmetry [61,62], which forces the symmetry of the energy spectrum of $\mathcal{H}(\mathbf{k})$ relative to zero energy. The parameters used are $m = 0.5$ eV, $M = 1$ eV, $c = 1$ eV. When the exchange field is applied, the time-reversal symmetry is destroyed in the system, and the other symmetries are preserved. The Hamiltonian in Eq. (1) transfers as

$$\mathcal{T}\mathcal{H}(\mathbf{k})\mathcal{T}^{-1} \neq \mathcal{H}(-\mathbf{k}), \quad (3)$$

$$\mathcal{P}\mathcal{H}(\mathbf{k})\mathcal{P}^{-1} = \mathcal{H}(-\mathbf{k}), \quad (4)$$

$$\mathcal{M}_z\mathcal{H}(k_x, k_y, k_z)\mathcal{M}_z^{-1} = \mathcal{H}(k_x, k_y, -k_z), \quad (5)$$

$$\mathcal{C}\mathcal{H}(k_x, k_y)\mathcal{C}^{-1} = -\mathcal{H}(k_x, k_y). \quad (6)$$

For further calculation, we discretize the low-energy effective model in Eq. (1) on a cubic lattice with lattice constant $a$ along the three orthogonal directions. The low-energy Hamiltonian $\mathcal{H}(\mathbf{k})$ around the $\Gamma$ point in the Brillouin zone can be expressed as [51]

$$\mathcal{H} = \sum c_i^\dagger H_0 c_i + \sum c_i^\dagger H_x c_{i+x} + \sum c_i^\dagger H_y c_{i+y} \sum c_i^\dagger H_z c_{i+z} + \text{H.c.}, \quad (7)$$

where

$$H_0 = (mc^2 - 6M)\tau_z \otimes \sigma_0 + B\tau_z \otimes \sigma_z, \quad (8)$$

$$H_x = M\tau_z \otimes \sigma_0 - i\frac{c}{2}\tau_x \otimes \sigma_x, \quad (9)$$

$$H_y = M\tau_z \otimes \sigma_0 - i\frac{c}{2}\tau_x \otimes \sigma_y, \quad (10)$$

$$H_z = M_a\tau_z \otimes \sigma_0 - i\frac{c_a}{2}\tau_x \otimes \sigma_z. \quad (11)$$

Here, $i = x, y, z$ for lattice discretization, $c_i^\dagger(c_i)$ is the creation (annihilation) operator. Using this lattice Hamiltonian

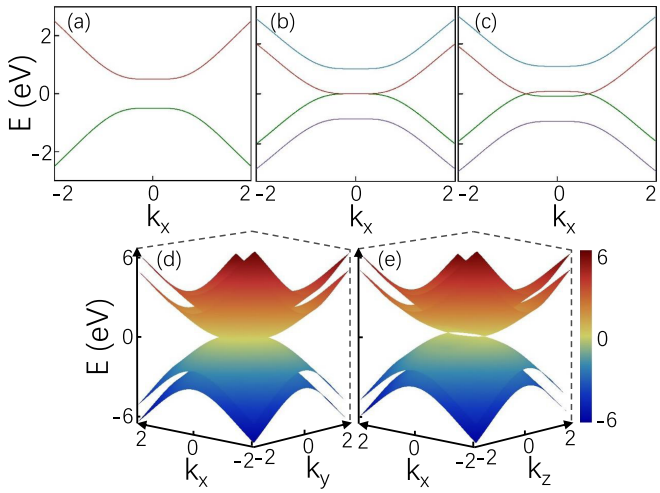


FIG. 2. (a)–(c) The bulk energy band structures for the Hamiltonian in Eq. (1) plotted as a function of $k_x$. (a) Topological insulator with $B = 0$ eV, (b) nodal point semimetal with $B = 0.5$ eV and (c) NLSM with $B = 0.6$ eV. (d), (e) The NLSM low-energy band structure of Hamiltonian in Eq. (1) in two selected planes with $B = 0.6$ eV. (d) and (e) show the energy band structures in the planes of $k_z = 0$ and $k_y = 0$, respectively. Here we choose parameters $m = 0.5$ eV, $M = 1$ eV, $c = 1$ eV at $k_z = 0$.

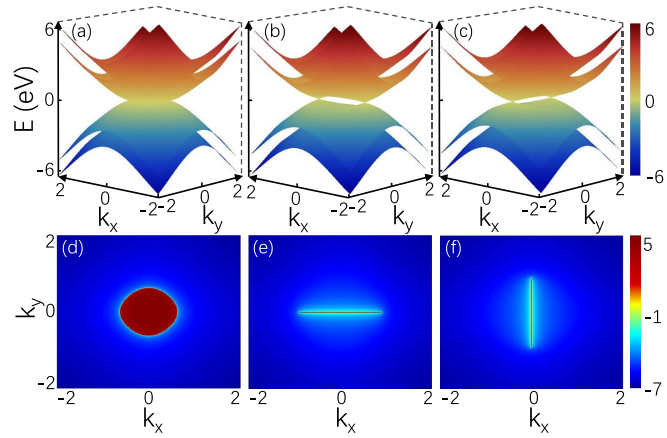


FIG. 3. (a) The three-dimensional (3D) band structure of the Hamiltonian in Eq. (14) with perturbation terms $H_{\delta_1} = 0$ and the nodal line in the $k_x$-$k_y$ plane protected by the mirror symmetry. (b) The 3D band structure with the perturbation term $H_{\delta_1} = 0.6$, where the nodal ring of the $k_x$-$k_y$ plane gaps out and create two Weyl points along the $k_x$ axis. (c) The 3D band structure with the perturbation term $H_{\delta_2} = 0.6$, where two Weyl points along the $k_y$ axis. (d)–(f) The NLAM corresponding drumhead surface state and the Fermi arcs connecting Weyl points with opposite chirality at the chemical potential of $E = 0$ eV on the [001] side surface for the same parameters as (a)–(c). Here we choose parameters $m = 0.5$ eV, $M = 1$ eV, $c = 1$ eV, and $B = 0.6$ eV.

in Eq. (7), the energy spectrum and surface state density can be obtained conveniently. We show the bulk phase transitions of exchange field modulation $B$ in Fig. 2. Figure 2(a) shows the topological insulator for $B = 0$ eV. Due to the existence of time-reversal and inversion symmetry, these bands are doubly degenerate. When the exchange field is applied, the time-reversal symmetry is broken, and the spin degeneracy is lifted. The critical point $B = 0.5$ eV, when the valence band and conduction band overlap at one point to form a nodal-point semimetal is shown in Fig. 2(b). When the exchange field $B > 0.5$ eV, the valence band and conduction band are further overlapped to form a closed ring in the $k_x$-$k_y$ plane, which is a NLSM. Figure 2(c) illustrates the NLSM for $B = 0.6$ eV. Figures 2(d) and 2(e) show the energy dispersions of the four bands in the $k_x$-$k_y$ plane with $k_z = 0$ and in the $k_x$-$k_z$ plane with $k_y = 0$, respectively. The energy band structures of NLSM are anisotropic. The $k_x$-$k_y$ plane presents a nodal ring, but the $k_x$-$k_z$ plane has two Weyl cones. The nodal line is protected by the mirror symmetry $\mathcal{M}_z$ (in the $k_x$-$k_y$ plane). Next, we discuss adding different perturbation terms to break the corresponding symmetries, and realize the nodal rings of the $k_x$-$k_y$ plane to form Weyl points in different directions.

## III. TOPOLOGICAL PHASE TRANSITION CAUSED BY BREAKING THE MIRROR SYMMETRY

In this system, the nodal ring of the $k_x$-$k_y$ plane is protected by the mirror symmetry $\mathcal{M}_z$. When the mirror symmetry is broken, the nodal line gaps out and generates Weyl points along the $k_x$ axis or along the $k_y$ axis to form WSM. We show that the mirror symmetry can be broken by adding disturbances, and the nodal ring forms Weyl points as shown in Fig. 3. We consider adding the following two kinds of disturbances:

$$H_{\delta_1} = \delta_1 \tau_0 \otimes \sigma_x, \tag{12}$$

and

$$H_{\delta_2} = \delta_2 \tau_0 \otimes \sigma_y. \tag{13}$$

Here, $\delta_1$ and $\delta_2$ represent the perturbation intensities.

The Hamiltonian with the perturbation term $H_{\delta_1}$ as follows:

$$\mathcal{H}_{\delta_1}(\mathbf{k}) = \mathcal{H}(\mathbf{k}) + \delta_1 \tau_0 \otimes \sigma_x. \tag{14}$$

The energy spectra of $\mathcal{H}_{\delta_1}(\mathbf{k})$ is given by

$$E_{s,r,\delta_1}(\mathbf{k}) = s\Big[B^2 - \delta_1^2 + (mc^2 - M\mathbf{k}^2)^2 + c^2\mathbf{k}^2 + 2r \times \sqrt{\big(B^2 - \delta_1^2\big)(mc^2 - M\mathbf{k}^2)^2 + B^2c^2\big(k_x^2 + k_y^2\big) - c^2\delta_1^2 k_y^2}\Big]^{\frac{1}{2}}, \tag{15}$$

where $s = \pm$, $r = \pm$. According to the transformations, the Hamiltonian Eq. (14) respects the inversion symmetry and the chiral symmetry, but breaks the mirror symmetry such that $\mathcal{P}\mathcal{H}_{\delta_1}(\mathbf{k})\mathcal{P}^\dagger = \mathcal{H}_{\delta_1}(-\mathbf{k})$, $\mathcal{C}\mathcal{H}_{\delta_1}(k_x, k_y)\mathcal{C}^{-1} = -\mathcal{H}_{\delta_1}(k_x, k_y)$, $\mathcal{M}_z\mathcal{H}_{\delta_1}(k_x, k_y, k_z)\mathcal{M}_z^\dagger \neq \mathcal{H}_{\delta_1}(k_x, k_y, -k_z)$. Therefore, the nodal ring of the $k_x$-$k_y$ plane protected by the mirror symmetry gaps out and creates Weyl points along the $k_x$ axis, as shown in Fig. 3. It is straightforward to check that the band dispersion Eq. (15) touch at two Weyl points, the positions are $\mathbf{k}^w = (\pm p_1, 0, 0)$, $p_1 \approx 0.967$. As can be seen

from Fig. 3(a), when the perturbation term $H_{\delta_1} = 0$, the model system is a NLSM with the nodal ring of the $k_x$-$k_y$ plane, while for $H_{\delta_1} > 0$ in Fig. 3(b), it is transformed into WSM phase, and a pair of Weyl points appear on the $k_x$ axis. Both the NLSM and the WSM have topologically protected surface states. The corresponding surface states can be obtained by using the iterative method to calculate the surface Green's function $G(\mathbf{k})$ of the semi-infinite system [63,64],

$$G(\mathbf{k}) = (E - H_0 - H_1 T)^{-1}. \tag{16}$$

Here, $H_0$ ($H_1$) is single-layer (interlayer coupling) Hamiltonian matrix element, $T$ is inverse matrix. The local density of states is the imaginary part of the Green's function $G(\mathbf{k})$, which is given as

$$A(\mathbf{k}) = -\frac{1}{\pi} ImTr[G(\mathbf{k})]. \tag{17}$$

We show the evolution of the surface states on the [001] side surface in Figs. 3(d) and 3(e). The NLSM corresponding drumhead surface state flat at the chemical potential of $E = 0$ eV with $H_{\delta_1} = 0$ in the $k_x$-$k_y$ plane is shown in Fig. 3(d). Figure 3(e) shows the Fermi arcs connecting Weyl points with opposite chirality when Fermi energy values $E_F = 0$ with $H_{\delta_1} = 0.6$. As perturbation term $H_{\delta_1}$ is turned to zero, the Fermi arc is transformed into the drumhead surface state in Fig. 3(d).

The Hamiltonian with the latter perturbation term $H_{\delta_2}$ as follows:

$$\mathcal{H}_{\delta_2}(\mathbf{k}) = \mathcal{H}(\mathbf{k}) + \delta_2 \tau_0 \otimes \sigma_y. \tag{18}$$

The energy spectra of $\mathcal{H}_{\delta_2}(\mathbf{k})$ is given by

$$E_{s,r,\delta_2}(\mathbf{k}) = s\Big[B^2 + \delta_2^2 + (mc^2 - M\mathbf{k}^2)^2 + c^2\mathbf{k}^2 + 2r \times \sqrt{\big(B^2 + \delta_2^2\big)(mc^2 - M\mathbf{k}^2)^2 + B^2c^2\big(k_x^2 + k_y^2\big) + c^2\delta_2^2 k_y^2}\Big]^{\frac{1}{2}}, \tag{19}$$

where $s = \pm$, $r = \pm$. The Hamiltonian Eq. (18) also hosts two Weyl points and breaks mirror symmetry but preserves inversion symmetry and chiral symmetry. The difference from the result caused by the perturbation term $H_{\delta_1}$ is that the two Weyl points generated by $H_{\delta_2}$ are along the $k_y$ axis. Evaluating the band dispersion $E_{s,r,\delta_2}(\mathbf{k}) = 0$, we can get the positions of the two Weyl points at $\mathbf{k}^w = (0, \pm p_2, 0)$, $p_2 \approx 0.967$. Figure 3(c) shows the positions of two Weyl points along the $k_y$ axis in the Brillouin zone with the perturbation term $H_{\delta_2} = 0.6$. Figure 3(f) shows the Fermi arcs connecting Weyl points along the $k_y$ axis with opposite chirality onto the [001] side surface at the Fermi energy $E_F = 0$ eV.

Through the above study, we find that both perturbation term $H_{\delta_1}$ and $H_{\delta_2}$ can break the mirror symmetry and realize the transformation from NLSM to WSM. Moreover, the perturbation term $H_{\delta_1}$ and $H_{\delta_2}$ break the nodal line in the $k_x$-$k_y$ plane and generate Weyl points along the $k_x$ axis and Weyl points along the $k_y$ axis, respectively.

## IV. TOPOLOGICAL PHASE TRANSITION CAUSED BY BREAKING THE EMERGENT CHIRAL SYMMETRY

Next, we add another perturbation term to achieve the transition from NLSM to WSM. Compared with the previous study in this paper, the different is that the Weyl points are not in the $k_x$-$k_y$ plane, but along the $k_z$ axis. Moreover, in the process of adjusting the perturbation term, we realized a series of nontrivial topological phases.

We consider adding the following perturbation term to the Hamiltonian Eq. (1):

$$H_{\delta_3} = \delta_3 \tau_0 \otimes \sigma_z. \tag{20}$$

With the perturbation term $H_{\delta_3}$, the Hamiltonian of the system can be written as

$$\mathcal{H}_{\delta_3}(\mathbf{k}) = \mathcal{H}(\mathbf{k}) + \delta_3 \tau_0 \otimes \sigma_z, \tag{21}$$

where $\delta_3$ represents the perturbation intensity. The Hamiltonian Eq. (21) is invariant under the inversion and mirror inversion symmetries, but does not satisfy the chiral symmetry. The Hamiltonian in Eq. (21) transfers as $\mathcal{P}\mathcal{H}_{\delta_3}(\mathbf{k})\mathcal{P}^\dagger = \mathcal{H}_{\delta_3}(-\mathbf{k})$, $\mathcal{M}_z\mathcal{H}_{\delta_3}(k_x, k_y, k_z)\mathcal{M}_z^\dagger = \mathcal{H}_{\delta_3}(k_x, k_y, -k_z)$, and $\mathcal{C}\mathcal{H}_{\delta_3}(k_x, k_y)\mathcal{C}^{-1} \neq -\mathcal{H}_{\delta_3}(k_x, k_y)$. The chiral symmetry makes the energy spectrum symmetrical with respect to zero energy. Breaking the chiral symmetry leads to the gradual bending of the energy bands, resulting in a series of topological phase transitions.

The evolution of the nodal line of the $k_x$-$k_y$ plane with $k_z = 0$ are shown in Fig. 4. With the increase of the perturbation term $H_{\delta_3}$, the nodal line decreases gradually. And the valence band and conduction band near the nodal ring have the same slope sign, evolving into the type-II NLSM [65,66], as shown in Figs. 4(a) and 4(e) with $H_{\delta_3} = 0.3$. When the perturbation term increases to $H_{\delta_3} = 0.6$, the nodal ring shrink to a point, as seen in Figs. 4(b) and 4(f). After that, the energy level opens the gap. Figures 4(c) and 4(g) shows that the point is gapped out when the perturbation term $H_{\delta_3} = 1$, but the bottom of the conduction band is below the Fermi energy $E_F = 0$ eV. When the perturbation term $H_{\delta_3} = 2$, the Fermi energy $E_F = 0$ eV across the energy gap, as seen in Figs. 4(d) and 4(h).

The evolution of the Weyl cones of the $k_x$-$k_z$ plane in Fig. 2(e) is shown in Fig. 5. In Fig. 2(e), the two Weyl points are along the $k_x$ direction. As the perturbation term $H_{\delta_3}$ increases, the positions of the two Weyl points on $k_x$ axis are gradually approaching in Figs. 5(a) and 5(e). When $H_{\delta_3} = 0.6$, two Weyl points shrink into a point as show in Figs. 5(b) and 5(f) the same as Figs. 4(b) and 4(f). At this time, the system is isotropic. The point splits into two Weyl points along the $k_z$ direction when $H_{\delta_3} > 0.6$. Two tilted Weyl cones are generated along the $k_z$ direction, transforming into type-II WSM with $H_{\delta_3} = 1$ [19,67], as shown in Figs. 5(c) and 5(g). The Weyl points lie about $E = 0.14$ eV above the Fermi energy. When $H_{\delta_3} = 2$, the system is transformed into type-I WSM with two Weyl points along the $k_z$ direction in Figs. 5(d) and 5(h). The Weyl points lie about $E = 0.5$ eV above the Fermi energy.

The above study shows that the perturbation term $H_{\delta_3}$ breaks the chiral symmetry and transforms the nodal

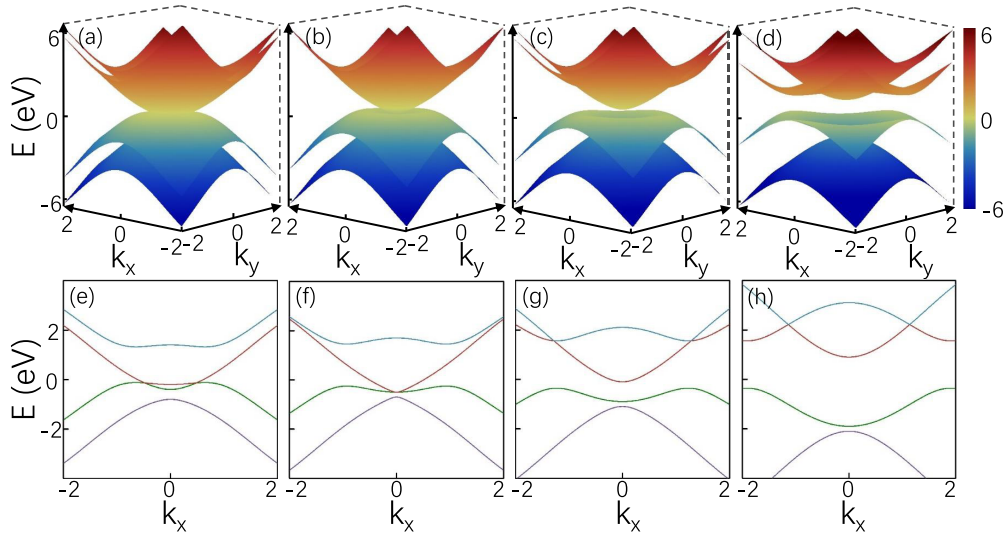


FIG. 4. Bulk band structure for the Hamiltonian in Eq. (21) in the plane of $k_z = 0$. (a)–(d) The 3D energy dispersions for the $\mathcal{H}_{\delta_3}(\mathbf{k})$. Here we have chosen parameters $k_z = 0$ with parameters $m = 0.5$ eV, $M = 1$ eV, $c = 1$ eV, and $B = 0.6$ eV. (a) The nodal line gradually shrinks and evolved into the type-II NLSM when perturbation term $H_{\delta_3} = 0.3$. (b) The critical point of the nodal line of the $k_x$-$k_y$ plane disappear with $H_{\delta_3} = 0.6$. (c) The energy bands be gapped out with $H_{\delta_3} = 1$, but the bottom of the conduction band is below the Fermi energy $E_F = 0$ eV. (d) The energy gap increases, and the Fermi energy $E_F = 0$ eV passes through the energy gap with $H_{\delta_3} = 2$. (e)–(h) Bulk band structure cuting through the nodal line at $k_y = k_z = 0$ for the same parameters as (a)–(e).

semimetal with the nodal ring on the $k_x$-$k_y$ plane into the Weyl semimetal with two Weyl points along the $k_z$ direction. And in the process of adjusting the perturbation term $H_{\delta_3}$, with the evolution of the energy bands, the type-II NLSM, the type-II WSM, and the type-I WSM have been realized successively. Next we focus on the surface state density of the type-II NLSM, the type-II WSM, and the type-I WSM produced during topological phase transition on the [010] side surface by using the iterative method to calculate the Green's function of the semi-infinite system, as shown in Fig. 6. In Fig. 6(a), we show the electron pocket and hole pocket of type-II NLSM near the nodal line ($E = -0.145$ eV), and the drum-head surface state flat like in Fig. 3(d) disappears. In type-II NLSM, the bulk states have a closed nodal line but the cones on the closed nodal line become tilted. Therefore, in the surface state density projection diagram near the nodal

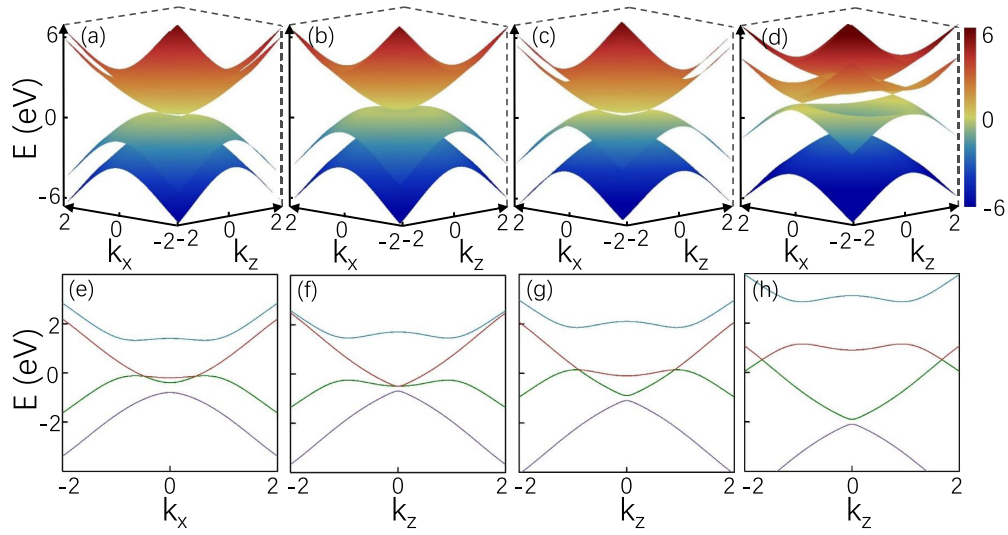


FIG. 5. Bulk band structure for the Hamiltonian in Eq. (21) in the plane of $k_y = 0$. (a)–(d) The 3D energy dispersions for the $\mathcal{H}_{\delta_3}(\mathbf{k})$. Here we have chosen parameters $k_y = 0$ with parameters $m = 0.5$ eV, $M = 1$ eV, $c = 1$ eV, and $B = 0.6$ eV. (a) The two Weyl points along the $k_x$ direction are getting closer when perturbation term $H_{\delta_3} = 0.3$. (b) The critical point of the two Weyl points shrink into a point with $H_{\delta_3} = 0.6$. (c) Two tilted Weyl cones are generated along the $k_z$ direction with $H_{\delta_3} = 1$, transforming into type-II WSM. (d) When $H_{\delta_3} = 2$, the system is transformed into type-I WSM with two Weyl points along the $k_z$ direction. (e) Bulk band structure cutting through the Weyl nodes at $k_y = k_z = 0$ for the same parameters as (a). (f)–(h) Bulk band structure cutting through the Weyl nodes at $k_x = k_y = 0$ for the same parameters as (b)–(e).

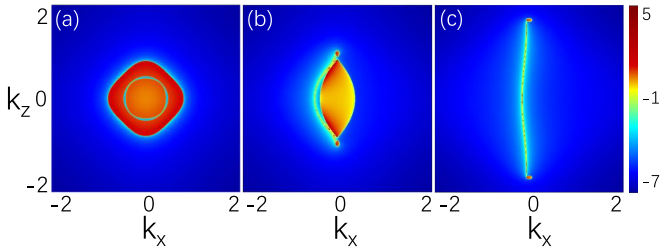


FIG. 6. The surface state density of type-II NLSM, type-II WSM, and type-I WSM produced during topological phase transition with $H_{\delta_3}$ on the [010] surface. (a) The surface state density of type-II NLSM with $H_{\delta_3} = 0.3$ at $E = -0.145$ eV. (b) The Fermi arc of type-II WSM with $H_{\delta_3} = 1$ at $E = 0.135$ eV. (c) The Fermi arc of type-I WSM with $H_{\delta_3} = 2$ at $E = 0.45$ eV. Here we choose parameters $m = 0.5$ eV, $M = 1$ eV, $c = 1$ eV, and $B = 0.6$ eV.

line, the inside of the surface state is the electron pocket and the outside is the hole pocket. In Fig. 6(b), we can see the electron and hole pockets and Fermi arc at $E$ passes near the Weyl points ($E = 0.135$ eV). The Weyl cones are completely inclined, so electron and hole pockets can coexist at certain energy level. Consistent with the type-II WSM bulk band structure, the electron pocket is located in the middle of the two Weyl points, and the hole pockets appear on both sides. The Fermi arc starts at one Weyl point and ends near another Weyl point. In Fig. 6(c), we show the electron pockets and a Fermi arc connecting two Weyl points of the type-I WSM at $E$ passes near the Weyl points ($E = 0.45$ eV).

## V. DISCUSSION AND SUMMARY

In this work, we theoretically study the topological phase transition and the energy band evolution of the NLSM caused by the destructions of the mirror symmetry and the emergent chiral symmetry. This NLSM is achieved by adding the exchange field $B$ to the topological insulator to break the time-reversal symmetry [51]. The nodal line in the $k_x$-$k_y$ plane is protected by the mirror reflection symmetry $\mathcal{M}_z$. First, we add the perturbation terms $H_{\delta_1}$ and $H_{\delta_2}$ that break $\mathcal{M}_z$ to produce the WSMs with the Weyl points along the $k_x$ axis and the $k_y$ axis, respectively. We further study the addition of the perturbation term $H_{\delta_3}$ to destroy the chiral symmetry to realize the topological phase transition. As the perturbation term $H_{\delta_3}$ increases, the energy bands bend and the nodal ring within the $k_x$-$k_y$ plane gradually shrinks and moves away from the Fermi level $E_F = 0$. With the evolution of the energy bands, the type-II NLSM are realized at the perturbation term $H_{\delta_3} = 0.3$. When $H_{\delta_3} = 0.6$, the nodal ring shrinks to a nodal point. Most remarkably, when $H_{\delta_3} > 0.6$, two Weyl points split along the $k_z$ axis, and the Weyl cones are inclined. As perturbation term increases, the system transforms to the type-II WSM and the positions of the Weyl points are above the Fermi level with $H_{\delta_3} = 1$. When the perturbation term $H_{\delta_3}$ continues to increase, the system transforms to the type-I WSM and the Weyl points are located at higher energy level with $H_{\delta_3} = 2$. In the above presentations, we not only generate the WSMs with the Weyl points on the $k_x$-$k_y$ plane where the nodal ring is located, but also produce the WSM with the Weyl points on the $k_z$ axis. Furthermore, we calculate the surface state density to demonstrate that type-II NLSM, type-I, and type-II WSMs can be realized by introducing the perturbation term $H_{\delta_3}$. Our results provides a wealth of methods to realize the topological phase transition of NLSM and WSM, and is also expected to be used in related topological applications due to its interesting characteristics.

## ACKNOWLEDGMENT

This work was financially supported by the Beijing Natural Science Foundation (Z180007).

[1] K. S. Novoselov, A. K. Geim, S. V. Morozov, D. Jiang, Y. Zhang, S. V. Dubonos, I. V. Grigorieva, and A. A. Firsov, Electric field effect in atomically thin carbon films, Science **306**, 666 (2004).

[2] K. S. Novoselov, A. K. Geim, S. V. Morozov, D. Jiang, M. I. Katsnelson, I. V. Grigorieva, S. V. Dubonos, and A. A. Firsov, Two-dimensional gas of massless Dirac fermions in graphene, Nature (London) **438**, 197 (2005).

[3] M. I. Katsnelson, K. S. Novoselov, and A. K. Geim, Chiral tunnelling and the Klein paradox in graphene, Nat. Phys. **2**, 620 (2006).

[4] A. H. Castro Neto, F. Guinea, N. M. R. Peres, K. S. Novoselov, and A. K. Geim, The electronic properties of graphene, Rev. Mod. Phys. **81**, 109 (2009).

[5] M. Z. Hasan and C. L. Kane, Colloquium: Topological insulators, Rev. Mod. Phys. **82**, 3045 (2010).

[6] X. L. Qi and S. C. Zhang, Topological insulators and superconductors, Rev. Mod. Phys. **83**, 1057 (2011).

[7] Z. Wang, Y. Sun, X.-Q. Chen, C. Franchini, G. Xu, H. Weng, X. Dai, and Z. Fang, Dirac semimetal and topological phase transitions in $A_3Bi$(A = Na, K, Rb), Phys. Rev. B **85**, 195320 (2012).

[8] Z. K. Liu, B. Zhou, Y. Zhang, Z. J. Wang, H. M. Weng, D. Prabhakaran, S.-K. Mo, Z. X. Shen, Z. Fang, X. Dai, Z. Hussain, and Y. L. Chen, Discovery of a three-dimensional topological dirac semimetal, $Na_3Bi$, Science **343**, 864 (2014).

[9] S.-M. Huang, S.-Y. Xu, I. Belopolski, C.-C. Lee, G. Chang, B. Wang, N. Alidoust, G. Bian, M. Neupane, C. Zhang, S. Jia, A. Bansil, H. Lin, and M. Z. Hasan, A Weyl Fermion semimetal with surface Fermi arcs in the transition metal monopnictide TaAs class, Nat. Commun. **6**, 7373 (2015).

[10] H. Weng, C. Fang, Z. Fang, B. A. Bernevig, and X. Dai, Weyl Semimetal Phase in Noncentrosymmetric Transition-Metal Monophosphides, Phys. Rev. X **5**, 011029 (2015).

[11] B. Q. Lv, N. Xu, H. M. Weng, J. Z. Ma, P. Richard, X. C. Huang, L. X. Zhao, G. F. Chen, C. E. Matt, F. Bisti, V. N. Strocov, J. Mesot, Z. Fang, X. Dai, T. Qian, M. Shi, and H. Ding, Observation of Weyl nodes in TaAs, Nat. Phys. **11**, 724 (2015).

[12] H. Gao, J. W. Venderbos, Y. Kim, and A. M. Rappe, Topological semimetals from first principles, Annu. Rev. Mater. Sci. **49**, 153 (2019).

[13] M. Neupane, S.-Y. Xu, R. Sankar, N. Alidoust, G. Bian, C. Liu, I. Belopolski, T.-R. Chang, H.-T. Jeng, H. Lin, A. Bansil, F. Chou, and M. Z. Hasan, Observation of a three-dimensional topological Dirac semimetal phase in high-mobility $Cd_3As_2$, Nat. Commun. **5**, 3786 (2014).

[14] J. A. Steinberg, S. M. Young, S. Zaheer, C. L. Kane, E. J. Mele, and A. M. Rappe, Bulk Dirac Points in Distorted Spinels, Phys. Rev. Lett. **112**, 036403 (2014).

[15] B.-J. Yang and N. Nagaosa, Classification of stable three-dimensional Dirac semimetals with nontrivial topology, Nat. Commun. **5**, 4898 (2014).

[16] H. Li, H. He, H. Z. Lu, H. Zhang, H. Liu, R. Ma, Z. Fan, S. Q. Shen, and J. Wang, Negative magnetoresistance in Dirac semimetal $Cd_3As_2$, Nat. Commun. **7**, 10301 (2016).

[17] L. Lu, Z. Wang, D. Ye, L. Ran, L. Fu, J. D. Joannopoulos, and M. Soljačić, Experimental observation of Weyl points, Science **349**, 622 (2015).

[18] S.-Y. Xu, I. Belopolski, N. Alidoust, M. Neupane, G. Bian, C. Zhang, R. Sankar, G. Chang, Z. Yuan, C.-C. Lee, S.-M. Huang, H. Zheng, D. S. Sanchez, B. Wang, A. Bansil, F. Chou, P. P. Shibayev, H. Lin, S. Jia, and M. Z. Hasan, Discovery of a Weyl fermion semimetal and topological Fermi arcs, Science **349**, 613 (2015).

[19] A. A. Soluyanov, D. Gresch, Z. Wang, Q. Wu, M. Troyer, X. Dai, and B. A. Bernevig, Type-II Weyl semimetals, Nature (London) **527**, 495 (2015).

[20] A. A. Burkov, M. D. Hook, and L. Balents, Topological nodal semimetals, Phys. Rev. B **84**, 235126 (2011).

[21] R. Yu, H. Weng, Z. Fang, X. Dai, and X. Hu, Topological Node-Line Semimetal and Dirac Semimetal State in Antiperovskite $Cu_3PdN$, Phys. Rev. Lett. **115**, 036807 (2015).

[22] Y. Kim, B. J. Wieder, C. L. Kane, and A. M. Rappe, Dirac Line Nodes in Inversion-Symmetric Crystals, Phys. Rev. Lett. **115**, 036806 (2015).

[23] Q. Xu, R. Yu, Z. Fang, X. Dai, and H. Weng, Topological nodal-line semimetals in the $CaP_3$ family of materials, Phys. Rev. B **95**, 045136 (2017).

[24] R. Yu, Q. Wu, Z. Fang, and H. Weng, From Nodal Chain Semimetal to Weyl Semimetal in HfC, Phys. Rev. Lett. **119**, 036401 (2017).

[25] C. Zhong, Y. Chen, Y. Xie, S. A. Yang, M. L. Cohen, and S. B. Zhang, Towards three-dimensional Weyl-surface semimetals in graphene networks, Nanoscale **8**, 7232 (2016).

[26] Q.-F. Liang, J. Zhou, R. Yu, Z. Wang, and H. Weng, Nodesurface and node-line fermions from nonsymmorphic lattice symmetries, Phys. Rev. B **93**, 085427 (2016).

[27] O. Türker and S. Moroz, Weyl nodal surfaces, Phys. Rev. B **97**, 075120 (2018).

[28] W. Wu, Y. Liu, S. Li, C. Zhong, Z.-M. Yu, X.-L. Sheng, Y. X. Zhao, and S. A. Yang, Nodal surface semimetals: Theory and material realization, Phys. Rev. B **97**, 115125 (2018).

[29] X. Zhang, Z.-M. Yu, Z. Zhu, W. Wu, S.-S. Wang, X.-L. Sheng, and S. A. Yang, Nodal loop and nodal surface states in the $Ti_3Al$ family of materials, Phys. Rev. B **97**, 235150 (2018).

[30] C.-K. Chiu, J. C. Y. Teo, A. P. Schnyder, and S. Ryu, Classification of topological quantum matter with symmetries, Rev. Mod. Phys. **88**, 035005 (2016).

[31] B. Yan and C. Felser, Topological materials: Weyl semimetals, Annu. Rev. Condens. Matter Phys. **8**, 337 (2017).

[32] N. P. Armitage, E. J. Mele, and A. Vishwanath, Weyl and Dirac semimetals in three-dimensional solids, Rev. Mod. Phys. **90**, 015001 (2018).

[33] H. Weng, Y. Liang, Q. Xu, R. Yu, Z. Fang, X. Dai, and Y. Kawazoe, Topological node-line semimetal in three-dimensional graphene networks, Phys. Rev. B **92**, 045108 (2015).

[34] L. S. Xie, L. M. Schoop, E. M. Seibel, Q. D. Gibson, W. Xie, and R. J. Cava, A new form of $Ca_3P_2$ with a ring of Dirac nodes, APL Mater. **3**, 083602 (2015).

[35] Y.-H. Chan, C.-K. Chiu, M. Y. Chou, and A. P. Schnyder, $Ca_3P_2$ and other topological semimetals with line nodes and drumhead surface states, Phys. Rev. B **93**, 205132 (2016).

[36] J. L. Lu, W. Luo, X. Y. Li, S. Q. Yang, J. X. Cao, X. G. Gong, and H. J. Xiang, Two-dimensional node-line semimetals in a honeycomb-kagome lattice, Chin. Phys. Lett. **34**, 057302 (2017).

[37] Y. Sun, Y. Zhang, C.-X. Liu, C. Felser, and B. Yan, Dirac nodal lines and induced spin Hall effect in metallic rutile oxides, Phys. Rev. B **95**, 235104 (2017).

[38] S. G. Xu, B. Zheng, H. Xu, and X. B. Yang, Ideal nodal line semimetal in a two-dimensional boron bilayer, J. Phys. Chem. C **123**, 4977 (2019).

[39] C. Xu, Y. Wang, R. Han, H. Tu, and Y. Yan, Topological node line semimetal state in two-dimensional tetragonal allotrope of Ge and Sn, New J. Phys. **21**, 033005 (2019).

[40] L. Liu, C. Wang, J. Li, X. Q. Chen, Y. Jia, and J.-H. Cho, Two-dimensional topological semimetal states in monolayer $Cu_2Ge$, $Fe_2Ge$, and $Fe_2Sn$, Phys. Rev. B **101**, 165403 (2020).

[41] L. M. Schoop, M. N. Ali, C. Straßer, A. Topp, A. Varykhalov, D. Marchenko, V. Duppel, S. S. P. Parkin, B. V. Lotsch, and C. R. Ast, Dirac cone protected by non-symmorphic symmetry and three-dimensional Dirac line node in ZrSiS, Nat. Commun. **7**, 11696 (2016).

[42] M. Neupane, I. Belopolski, M. M. Hosen, D. S. Sanchez, R. Sankar, M. Szlawska, S.-Y. Xu, K. Dimitri, N. Dhakal, P. Maldonado, P. M. Oppeneer, D. Kaczorowski, F. Chou, M. Z. Hasan, and T. Durakiewicz, Observation of topological nodal fermion semimetal phase in ZrSiS, Phys. Rev. B **93**, 201104(R) (2016).

[43] B. Feng, B. Fu, S. Kasamatsu, S. Ito, P. Cheng, C. C. Liu, Y. Feng, S. Wu, S. K. Mahatha, P. Sheverdyaeva *et al.*, Experimental realization of two-dimensional Dirac nodal line fermions in monolayer $Cu_2Si$, Nat. Commun. **8**, 1007 (2017).

[44] L. Gao, J.-T. Sun, J.-C. Lu, H. Li, K. Qian, S. Zhang, Y.-Y. Zhang, T. Qian, H. Ding, X. Lin *et al.*, Epitaxial growth of honeycomb monolayer CuSe with dirac nodal line fermions, Adv. Mater. **30**, 1707055 (2018).

[45] B. Feng, R.-W. Zhang, Y. Feng, B. Fu, S. Wu, K. Miyamoto, S. He, L. Chen, K. Wu, K. Shimada *et al.*, Discovery of Weyl Nodal Lines in a Single-Layer Ferromagnet, Phys. Rev. Lett. **123**, 116401 (2019).

[46] X. Wan, A. M. Turner, A. Vishwanath, and S. Y. Savrasov, Topological semimetal and Fermi-arc surface states in the electronic structure of pyrochlore iridates, Phys. Rev. B **83**, 205101 (2011).

[47] S.-Y. Yang, H. Yang, E. Derunova, S. S. P. Parkin, B. Yan, and M. N. Ali, Symmetry demanded topological nodal-line materials, Adv. Phys.: X **3**, 1414631 (2018).

[48] M. Hirayama, R. Okugawa, T. Miyake, and S. Murakami, Topological Dirac nodal lines and surface charges in fcc alkaline earth metals, Nat. Commun. **8**, 14022 (2017).

[49] A. Yamakage, Y. Yamakawa, Y. Tanaka, and Y. Okamoto, Line-node dirac semimetal and topological insulating phase in noncentrosymmetric pnictides CaAgX(X = P, As), J. Phys. Soc. Jpn. **85**, 013708 (2016).

[50] Y. Du, F. Tang, D. Wang, L. Sheng, E.-J. Kan, C.-G. Duan, S. Y. Savrasov, and X. Wan, CaTe: A new topological node-line and Dirac semimetal, npj Quantum Mater. **2**, 3 (2017).

[51] T. Rauch, H. N. Minh, J. Henk, and I. Mertig, Model for ferromagnetic Weyl and nodal line semimetals: Topological invariants, surface states, anomalous and spin Hall effect, Phys. Rev. B **96**, 235103 (2017).

[52] R. Wang, J. Z. Zhao, Y. J. Jin, Y. P. Du, Y. X. Zhao, H. Xu, and S. Y. Tong, Nodal line fermions in magnetic oxides, Phys. Rev. B **97**, 241111(R) (2018).

[53] Y. Jiao, F. Ma, C. Zhang, J. Bell, S. Sanvito, and A. Du, First-Principles Prediction of Spin-Polarized Multiple Dirac Rings in Manganese Fluoride, Phys. Rev. Lett. **119**, 016403 (2017).

[54] M. M. Hosen, G. Dhakal, K. Dimitri, P. Maldonado, A. Aperis, F. Kabir, C. Sims, P. Riseborough, P. M. Oppeneer, D. Kaczorowski *et al.*, Discovery of topological nodal-line fermionic phase in a magnetic material GdSbTe, Sci. Rep. **8**, 13283 (2018).

[55] T. L. He, X. M. Zhang, W. Z. Meng, L. Jin, X. F. Dai, and G. D. Liu, Topological nodal lines and nodal points in the antiferromagnetic material $\beta$-$Fe_2PO_5$, J. Mater. Chem. C **7**, 12657 (2019).

[56] T. L. He, X. M. Zhang, Y. Liu, X. F. Dai, L. Y. Wang, and G. D. Liu, Potential antiferromagnetic Weyl nodal line state in $LiTi_2O_4$ material, Phys. Rev. B **104**, 045143 (2021).

[57] S. Q. Shen, W. Y. Shan, and H. Z. Lu, Topological insulator and the Dirac equation, Spin **01**, 33 (2011).

[58] G. Xu, H. Weng, Z. Wang, X. Dai, and Z. Fang, Chern Semimetal and the Quantized Anomalous Hall Effect in $HgCr_2Se_4$, Phys. Rev. Lett. **107**, 186806 (2011).

[59] G. Chang, S.-Y. Xu, H. Zheng, B. Singh, C.-H. Hsu, G. Bian, N. Alidoust, I. Belopolski, D. S. Sanchez, S. Zhang, H. Lin, and M. Z. Hasan, Room-temperature magnetic topological Weyl fermion and nodal line semimetal states in half-metallic Heusler $Co_2TiX$ (X=Si, Ge, or Sn), Sci. Rep. **6**, 38839 (2016).

[60] J. Noky, Q. Xu, C. Felser, and Y. Sun, Large anomalous Hall and Nernst effects from nodal line symmetry breaking in $Fe_2MnX$ (X = P, As, Sb), Phys. Rev. B **99**, 165117 (2019).

[61] Y. Chen, Y.-M. Lu, and H.-Y. Kee, Topological crystalline metal in orthorhombic perovskite iridates, Nat. Commun. **6**, 6593 (2015).

[62] C.-K. Chiu and A. P. Schnyder, Classification of crystalline topological semimetals with an application to $Na_3Bi$, J. Phys.: Conf. Ser. **603**, 012002 (2015).

[63] M. P. L. Sancho, J. M. L. Sancho, and J. Rubio, Quick iterative scheme for the calculation of transfer matrices: Application to Mo (100), J. Phys. F **14**, 1205 (1984).

[64] M. P. L. Sancho, J. M. L. Sancho, J. M. L. Sancho, and J. Rubio, Highly convergent schemes for the calculation of bulk and surface Green functions, J. Phys. F **15**, 851 (1985).

[65] S. Li, Z.-M. Yu, Y. Liu, S. Guan, S.-S. Wang, X. Zhang, Y. Yao, and S. A. Yang, Type-II nodal loops: Theory and material realization, Phys. Rev. B **96**, 081106(R) (2017).

[66] Y. Gao, Y. Chen, Y. Xie, P.-Y. Chang, M. L. Cohen, and S. Zhang, A class of topological nodal rings and its realization in carbon networks, Phys. Rev. B **97**, 121108(R) (2018).

[67] T. M. McCormick, I. Kimchi, and N. Trivedi, Minimal models for topological Weyl semimetals, Phys. Rev. B **95**, 075133 (2017).